

Kinematics of the Narrow-Line Region in the Seyfert 2 Galaxy Mrk 3¹

Jose R. Ruiz², D.M. Crenshaw^{2,3}, S.B. Kraemer^{2,3}, G.A. Bower⁴, T.R. Gull³, J.B.
Hutchings⁵, M.E. Kaiser⁶, & D. Weistrop⁷

Received _____; accepted _____

¹Based on observations made with the NASA/ESA Hubble Space Telescope. STScI is operated by the Association of Universities for Research in Astronomy, Inc. under NASA contract NAS5-26555.

²Catholic University of America

³Laboratory for Astronomy and Solar Physics, NASA's Goddard Space Flight Center, Code 681, Greenbelt, MD 20771

⁴NOAO, 950 N. Cherry Street, Tucson, AZ 85726-6732

⁵Dominion Astrophysical Observatory, National Research Council of Canada, 5071 West Saanich Rd., Victoria, BC V8X 4M6, Canada

⁶Department of Physics & Astronomy, Johns Hopkins University, 3400 North Charles St., Baltimore, MD 21218

⁷Department of Physics, University of Nevada at Las Vegas, 4505 South Maryland Parkway, Las Vegas, NV 89154-4002

ABSTRACT

We present measurements of radial velocities for the narrow-line region (NLR) gas in the Seyfert 2 galaxy Mrk 3 out to ~ 1 kpc from the nucleus. The observations consist of two datasets, both using the Space Telescope Imaging Spectrograph (STIS) on board the *Hubble Space Telescope* (*HST*): 1) An [O III] slitless spectrum with the G430M grating of the inner $3''$ around the nucleus, and 2) a long-slit observation centered on the nucleus (PA = 71°) using the G430L grating and the $52'' \times 0''.1$ aperture. Our results produce radial velocity maps of the emission-line gas. These maps indicate general trends in the gas motion, which include: blueshifts and redshifts on either side of the nucleus, steep velocity rises from systemic up to $\sim \pm 700$ km s $^{-1}$ taking place in the inner $0''.3$ (0.8 kpc) both east and west of the nucleus, gradual velocity descents back to near-systemic values from $0''.3$ – $1''.0$, slightly uneven velocity amplitudes on each side of the nucleus, and narrow velocity ranges over the entire observed region.

When fitted to kinematic modeling programs for the NLR gas, the data clearly favor a model where the gas exists in a partially filled bicone, is accelerated radially away from the nucleus, and is followed by a constant deceleration (possibly due to collision with an ambient medium). This geometry and general kinematic model is in agreement with previous work done on the NLR gas of NGC 1068 and NGC 4151. On scales of hundreds of parsecs, we conclude that radial outflow may be a common feature of Seyfert galaxies.

Subject headings: galaxies:individual (Mrk 3) – galaxies: Seyfert

1. Introduction

In many Seyfert 2s, the clouds appear to lie in a biconical or roughly linear configuration surrounding the nucleus (Schmitt & Kinney 1996, etc). Various kinematic models have been proposed to explain NLR cloud motion. Capetti et al. (1995) have compared optical and radio measurements of the NLR of Mrk 3 and concluded that the NLR clouds are the result of radio jet plasma expanding away from the bicone axis. Winge et al. (1997), (1999) postulate gravitational motions for the NLR in NGC 4151. Recently, Crenshaw & Kraemer (2000) and Kaiser et al. (2000) have determined radial velocities as a function of position in the NLRs of NGC 1068 and NGC 4151 (the brightest Seyfert 2 and Seyfert 1, respectively) with the STIS on *HST*. Crenshaw et al. (2000) have proposed a model where clouds on the surface of a bicone are radially accelerated from the nucleus by wind pressure or radiation pressure, encounter and collide with an ambient medium, then decelerate to near-systemic values. It explains the general trends seen in the radial velocity as a function of position in the inner kiloparsec around the nuclei of these galaxies.

Mrk 3 is a well-studied Seyfert 2 galaxy, which shows evidence for a hidden Seyfert 1 nucleus from broad polarized emission lines (Schmidt & Miller 1985). The host galaxy is classified as an elliptical or S0 galaxy type. It lies 53 Mpc away ($H_0=75 \text{ km s}^{-1} \text{ Mpc}^{-1}$, $z=0.0135$, $3.82'' \text{ kpc}^{-1}$). It has been studied in every wavelength regime, from the X-ray (Griffiths, 1998; Georgantopoulos et al, 1999) through the radio (Kukula et al. 1999). Mrk 3 has bright [O III] emission-line clouds that lie in a biconical configuration (apex of the two cones coincident with the nucleus) along $PA=80^\circ$, with a half-opening angle of 22.5° (Schmitt & Kinney 1996). At the end of the western cone, a large, diffuse knot appears, while on the end of the eastern cone, a bright knot appears out of the bicone, giving the entire structure an ‘S’ shape (Kukula et al. 1993). Schmitt & Kinney measure the clouds as extending 280 pcs on either side of the nucleus. Recent X-ray observations of Mrk 3 using

Chandra (Sako et al. 2000) have found soft X-ray extended emission which lies along this PA. Radio jets have also been observed (Axon et al. 1998, Kukula et al. 1999) along the same PA; these appear to follow the biconical structure, although the half-opening angle is far less ($\sim 8\text{-}10^\circ$). The jets also have an ‘S’ shape (though much less pronounced) in the same regions as the [O III] emission. Though they lie close to the emission-line clouds, they are not exactly coincident; Axon et al. (1998) suggest that they lie along the convex edge of the S-shaped curvature.

A fainter set of clouds, situated along P.A. $\sim 100^\circ$, are seen further out in the ENLR. These clouds extend from $1.''0$ on either side of the nucleus to about $3.''2$. This group is more diffuse, fainter in surface brightness by an order of magnitude, and follows the [O III] emission contour lines seen in the ground-based observations of Pogge & De Robertis (1993).

In this paper, we present two *HST* spectra (one long-slit, one slitless) of the Mrk 3 NLR clouds. They provide consistent values of radial velocities as functions of NLR cloud positions. The two datasets are then fitted to a kinematic modeling program that provides a radial velocity map of clouds within a bicone, given a velocity law that directs their motion. When fitted to the radial acceleration + constant deceleration velocity law, the trends seen in both datasets are matched well. In §2 we detail the observations, while the data analysis is presented in §3. The results from the two datasets are given in §4. The discussion of the model is given in §5, with §6 providing the overall discussion. §7 presents the conclusions.

2. Observations

In order to find the NLR knots in the slitless observations, and hence, determine their velocities, a companion [O III] image, as well as a continuum image are required. To

that end, the archival images of Mrk 3 were obtained. The first of these is a Wide Field Planetary Camera (WFPC) [O III] observation. This image served to match the bright NLR clouds. A Wide Field Planetary Camera 2 (WFPC 2) continuum image was also retrieved, as well as a Faint Object Camera (FOC) [O III] image. The FOC image is shown in Figure 1. It served to match the faint ENLR clouds. A summary of all the observations is given in Table 1.

The new slitless observations take advantage of STIS’s spatial resolution ($0''.1$) and the G430M spectral resolution ($\lambda/\Delta\lambda\approx 10,000$). The observations were centered at 5093 \AA , with a bandwidth of 286 \AA . In addition to [O III] $\lambda 5007$, [O III] $\lambda 4959$ and $H\beta$ were also observed. The spectral region around [O III] $\lambda 5007$ is shown in Fig. 2. The horizontal axis is the dispersion axis, while the vertical axis is the spatial axis, as indicated by the scale. The bright NLR clouds are smeared out along the dispersion axis, indicating large velocity dispersions. They are also shifted along this axis, from which their radial velocities can be calculated. The faint ENLR clouds are also seen with apparently smaller dispersions.

We also obtained long-slit observations of Mrk 3 using the G140L, G230L, G430L and G750L gratings and the $52'' \times 0''.1$ aperture. The complete observations covered the wavelength range from $1150\text{-}10,000 \text{ \AA}$. A full analysis of these data will be presented separately (Collins et al. 2001, in preparation). For this work, the single emission line of [O III] $\lambda 5007$ from these observations was used. The slit had a PA of 71° , and was chosen to pass through the nucleus. The position of the long-slit is shown in Fig. 1, overlaid on the FOC image for comparison with the [O III] clouds.

3. Data Analysis

The data reduction was done with IDL software developed for the STIS Instrument Definition Team at Goddard Space Flight Center (Lindler et al. 1999). The spectral images were cleaned of cosmic rays during the image processing. Once the archival images were retrieved, they were also cleaned of cosmic rays. Determining radial velocities of NLR clouds using slitless spectra has been done previously using NGC 4151 (Hutchings et al. 1998, Kaiser et al. 2000) and NGC 1068 (Crenshaw et al. 2000). These authors describe the STIS slitless data analysis; a brief synopsis follows here.

The data analysis consists of matching [O III] undispersed clouds (from an FOC, WFPC or WFPC2 image) with their counterparts in a STIS dispersed image. In order to make the one-to-one correspondence between clouds, the non-STIS images must be rotated, aligned, and corrected for anamorphic magnification with respect to the STIS image (spatial scale of $0''.0507 \text{ pixel}^{-1}$). Once the spatial scale is set, then the wavelength scale (ultimately a velocity scale) must be set using the calibration spectra. To set the velocity scale, the STIS dispersed image is aligned with the direct [O III] images such that there is no shift for a cloud at the systemic redshift ($z=0.0135$, Tift & Cooke 1988) of Mrk 3. The redshifted wavelength is taken from 21 cm measurements of H I, assumed to be at rest with respect to the central galactic region. We note that the WFPC [O III] observation and WFPC2 continuum image were taken at different times. Despite this, we were able to identify the bright, distinct emission line knots in both images.

Once the STIS dispersed image and the non-STIS undispersed image are aligned, Gaussian fits are made to the NLR knots in both images on each row parallel to the dispersion axis. This is to accurately determine the positions and FWHMs for each knot. The difference in position (in pixels) between an undispersed and dispersed knot is converted to a difference in \AA , then to one in velocity. The difference in width (in

quadrature) gives the velocity dispersion of the emission knot. For some purposes, the individual line measurements are averaged over each cloud in order to obtain a single value of radial velocity and dispersion, and the standard deviations are used as uncertainties.

For the long-slit data, Gaussian fits were made to the NLR knots on each row perpendicular to the dispersion (in $0''.05$ intervals). Once the positions and FWHMs were calculated, the radial velocities and dispersions for each row could be calculated using the same fitting routines as for the slitless spectrum. The FWHMs were corrected for the instrumental broadening of 300 km s^{-1} . For the purpose of comparing slitless and long slit data, we determined which clouds lay in the slit from the PA of the slit. We then averaged the long-slit radial velocities for these clouds over each individual cloud, thus obtaining two values of radial velocity from the two different methods and plotted them against each other. For both sets of radial velocities, the standard deviations calculated were used for the uncertainties. Figure 3 shows averaged slitless radial velocities plotted against the corresponding averaged long-slit radial velocities. The plot shows very good agreement, to within $\sim 50 \text{ km s}^{-1}$, indicating that there are no systematic errors with the slitless technique.

4. Results

The entire dataset is seen in Figure 4, which shows a plot of radial velocity versus distance. Each point represents an average over each cloud. The inner region clouds are seen to have a wide range of radial velocities, from -1000 km s^{-1} to $+600 \text{ km s}^{-1}$. There are roughly equal numbers of clouds that show redshifts and blueshifts. As noted in the previous section, the long-slit cloud values are consistent with the slitless spectral values, both in terms of location and velocity. The fainter, ENLR clouds stretch for about $1''.5$ further out in either direction than the inner region clouds. The fainter clouds show

a narrower range of radial velocity, from $+400 \text{ km s}^{-1}$ down to -200 km s^{-1} , with the majority of the clouds (75%) showing redshifts.

Figure 5 shows the velocity distribution of all the clouds. The NLR clouds are difficult to distinguish due to their proximity to each other, so we present this figure in order to show the ENLR clouds. The eastern half of these clouds is exclusively redshifted, while the majority of the western half is so with lower magnitudes. Figure 6 is an expanded view of the central region of Figure 5 to show the inner region clouds' velocity distribution in greater detail. The inner region clouds, in contrast to the extended region clouds, have equal numbers of blueshifted and redshifted clouds on either side of the nucleus. The blueshifted clouds to the east tend to have greater velocities, while to the west the velocities are similar for redshifts and blueshifts. On either side, maximum values of radial velocities are reached $\sim 0''.3$ away from the center for both sets of data.

Figure 7 shows the unbinned NLR radial velocities (relative to systemic) plotted against distance from the optical continuum center. The unbinned velocities are used for the model in order to take advantage of *HST's* spatial resolution. Long-slit points are shown, along with the slitless spectral points that lie within the slit. This set of points is used because the modeling program we use (to be discussed in the next section) simulates a long-slit, so we choose only those points within the slit. The velocity errors are only measurement errors in this case, and are comparable to the size of the symbols. The two sets of data points are seen to be compatible. They show properties that must be duplicated by any model fit. Now we briefly discuss each of these properties.

Both sets of data points show fast rises in velocities (from systemic values at the nucleus to $\sim \pm 600 \text{ km s}^{-1}$) out to $\sim 0''.25$ of the nucleus on each side. The climbs in velocities are seen in both redshifts and blueshifts. All the rises are then followed by shallower velocity downturns, so that at $\sim 0''.7-1''.0$, the velocities have returned to near systemic values. The

amplitudes of the maximum velocities are not equal. The amplitudes range from $\sim 300 \text{ km s}^{-1}$ on the blueshifted west side to $\sim 800 \text{ km s}^{-1}$ on the blueshifted east side (ignoring a few high-velocity points). This variation in amplitude implies that any fitted cone is tilted, and in fact, the angle of inclination can be calculated by the amplitude difference. Finally, the range of velocities is fairly narrow. For example, $\sim 0''.30$ west of the nucleus, blueshifted velocities are seen exclusively from -200 to -300 km s^{-1} , while redshifted velocities are seen spanning a narrow range from 300 to 500 km s^{-1} . At this distance, there are no velocities seen from -200 to 300 km s^{-1} . Any model fit must be able to match these narrow velocity ranges.

5. Model Fitting

Once the spatial orientations and radial velocities of the clouds were obtained, we attempted to fit these observations using kinematic modeling programs. These programs calculate the radial velocities and spectral lines of material on the surface of a thin disk, or a bicone, either filled or hollow. Each geometry can assume one of various velocity laws that control the material's movement. We concentrate here on the inner NLR out to $\sim 1''.0$ on either side of the nucleus. Later, we will discuss briefly the ENLR clouds and their motion.

We can immediately rule out gravitational rotation models by calculating the mass required to impart radial velocities on the order of $500\text{-}1000 \text{ km s}^{-1}$ at a distance of $100\text{-}200$ pcs away from the nucleus. This mass is of the order of $10^{9-10} M_{\odot}$. Typical masses for black holes in Seyfert nuclei are $10^{6-8} M_{\odot}$ (Peterson & Wandel 2000). Observationally, the observed morphology of the NLR does not suggest a disk geometry, while the redshifts and blueshifts on either side of the nucleus cannot be the result of simple Keplerian rotation. Thus we are left with outflow models, or models where material flows tangentially outward from the radio axis.

The bicone program has been used previously to model the NLR emission-line clouds of NGC 1068 and NGC 4151 (Crenshaw & Kraemer 2000, Crenshaw et al. 2000). The two cones (one on either side of the nucleus) are assumed to possess identical properties, including geometry, size and velocity law. In addition, the cones are assumed to have a filling factor of 1 within the minimum and maximum half opening angle, and not to absorb [O III] photons. We adjust certain parameters, shown in Table 2, to obtain the best fit. The program creates a two-dimensional velocity map, which is sampled through a simulated slit. We applied the models to unbinned velocities in order to obtain the best spatial resolution.

Several model input variables can be constrained from the observations. The first of these was the extent of the NLR. Based on the approximate placing of a bicone on the Mrk 3 NLR by Schmitt & Kinney (1996), we measured its maximum extent as $\sim 0.75''$. In addition to a minimum and maximum distance (in pixels) of the cones, the program requires a minimum and maximum half-opening angle. The maximum angle was measured from the images, giving a value of 25° . This agrees with Schmitt & Kinney (1996), who measure a maximum half-opening angle of 22.5° . The minimum half-opening angle is not visible in the [O III] images, so it was varied to match the data. The optimum value for the models was 15° . This value places the emission-line material outside the observed radio jet cone (half-opening angle $\sim 7\text{-}8^\circ$) (Capetti et al. 1995).

The inclination angle was calculated based on the differences between the radial velocity maxima on the W and E sides of the cones. The maximum blueshifts are higher by $\sim 300 \text{ km s}^{-1}$ than the maximum redshifts on the east side. The NLR inclination angle was then calculated as $\sim 5\text{-}10^\circ$, using simple trigonometry. Finally, the value for the maximum deprojected velocity of the NLR gas was chosen so that it would match the observed NLR radial velocity peak ($\sim 800 \text{ km s}^{-1}$). The best fit parameters of all the models are shown in Table 3. The results of the models are summarized below.

1. The radial acceleration (RA) outflow model consists of NLR clouds being driven away from the nucleus, perhaps by winds or jets. The acceleration is along the bicones' entire length. The best fit was not able to match the high velocities near the center, given the observed parameters. The only way to marginally match these velocities was to widen the half-opening angle past $\sim 40^\circ$, but the sharp downturns cannot then be fit. It is clear from the images that the ionization cone's half-opening angle cannot be more than $\sim 30^\circ$. If there is acceleration along the bicone, it cannot take place along the entire length of the NLR.

2. The constant velocity (CV) model consists of clouds with a negligible drag force, having been accelerated out to some distance (small compared to the NLR), then proceeding with constant velocity. This model is able to match the high central velocities $\sim 0''.3$ from the nucleus. Further out, however, the modeled velocities remain at a constant value out to the ENLR, whereas the observed velocities drop to near systemic values by $\sim 1''.0$ out from the center.

3. The constant tangential (CT) model consists of NLR clouds moving radially away from the central radio axis. This would be seen if the radio plasma expanded within the emission-line bicone. This fit resembles the CV model, except that it predicts equal magnitude redshifts and blueshifts on either side of the nucleus. This is certainly not the case, as seen in the two datasets. Note that this model predicts velocity magnitudes substantially less (1/3 to 1/6) than the other models (see Table 3). These velocities appear to be too low. There are a number of other inconsistencies with this model, which are discussed in §6.

4. The model that fit the most data points is the radial acceleration + constant deceleration (RA+CD). The model can be visualized as material first accelerated by wind or radiation pressure from the nucleus, which then impacts an ambient medium and then

decelerates at a constant rate. This model implies that the emission-line clouds originate from a region closer to the nucleus and move outward from there. Figure 8 shows the long-slit and slitless data points overlaid with the shading from this model. Obviously, this model does not perfectly fit every point, but it fits the gross features of the observations well. Many of the discrepant points can be ascribed to slightly different acceleration or deceleration laws in different quadrants. The discrepant high-velocity points suggest clouds that perhaps do not encounter the ambient, possibly patchy medium, or encounter it in a region of lower density and do not decelerate as much.

6. Discussion

The slitless spectral method of determining radial velocity gives consistent values with the long slit method, as shown in Figures 3 and 7. This result gives confidence in future work using the slitless method, and has been shown before for NGC 4151 (Hutchings et al. 1998, Crenshaw et al. 2000). The best fit RA+CD model shows, in addition to fitting all of the trends seen in the data, some discrepancies. These can best be explained by slightly different acceleration/deceleration laws in different directions.

While the NLR clouds are fitted most closely by the RA+CD model, the ENLR clouds require a different model. Those clouds (with velocities $\lesssim 350 \text{ km s}^{-1}$) appear to be influenced by the gravitational potential of the supermassive black hole (SMBH) and inner galaxy, rather than the outflowing material. This hypothesis agrees with surface photometry on Mrk 3 done by one of us (Bower). Ellipsoids were fit to the surface brightness of Mrk 3, from $0.01''$ out to $100''$. From these ellipsoid fits, a spherical dynamical model was used to predict a rough upper limit on the rotational radial velocity induced by the gravitational potential. For the range from $1''$ to $\sim 5''$, where the ENLR clouds reside, the projected radial velocities are predicted to be $\lesssim 200 \text{ km s}^{-1}$. This heuristic result agrees roughly with

the observed ENLR cloud velocities, although we cannot explain the preponderance of redshifted clouds with this model. They may be due to a lack of ionized gas at the positions that would produce blueshifts.

The orientation of the host galaxy has been previously reported as 27° out of the plane of the sky (Schmitt & Kinney 1996). If this orientation extends down to kiloparsec scales, then the plane of the galactic disk would lie within the angular range of one side of each cone (15° to 25° , tilted out 5° of the plane of the sky). The situation then resembles NGC 1068 and NGC 4151 (Crenshaw et al. 2000, Crenshaw & Kraemer 2000), which also seem to have the galactic disk and one side of the bicone in the same plane. Crenshaw et al. (2000) propose that the galactic disk’s ionization (by the nucleus) contributes to ENLR gas. We propose that the same geometry exists in this galaxy.

The radio jet and the NLR emission share a similar axis, and are nearly coincident. However, other than their spatial coincidence, there do not appear to be any other correlations, as would be expected if the radio plasma’s expansion were the source of the NLR velocities. Firstly, in the data itself, there are no bright NLR clouds that correspond to jet flux maxima. This lack of correspondence has been noted in other objects (NGC 4151, Kaiser et al. 2000). In addition, there is no evidence for peculiar velocities at the positions of the radio lobes. In terms of the dataset velocities, there is no physical reason given by this model to explain the velocity trends (increasing to some turnover distance, then steadily decreasing) that we see in the data. In terms of the modeling, the CT and other transverse velocity models, predict equal blueshift/redshift amplitudes no matter what inclination angle the bicone is tilted. The data show a definite difference (200-400 km s^{-1}) in velocity maxima between redshifts and blueshifts, consistent with a biconical geometry.

7. Conclusions

Two STIS spectra were obtained of the NLR of the Seyfert 2 galaxy Mrk 3. Radial velocities were determined of the emission-line gas as a function of position (out to ~ 1 kpc from the nucleus). The velocity maps indicate general trends in the gas motion. These include: blueshifts and redshifts on either side of the nucleus, steep velocity rises from systemic up to $\sim \pm 700$ km s $^{-1}$ taking place in the inner $0''.3$ (0.8 kpc) both east and west of the nucleus, and gradual velocity descents back to near-systemic values from $0''.3$ - $1''.0$.

The data were then fitted to kinematic modeling programs for the NLR gas on the surface of the bicone. The data sets were fit best with a radial acceleration + constant deceleration model. In the model, the cones extend out to a radius of $0''.75$ from the nucleus, with a half-opening angle between 15° and 25° . The modeled material reaches a maximum deprojected velocity of 1750 km s $^{-1}$, reaching this velocity at a distance of $0''.3$ - $0''.43$ from the nucleus, close to the observed distance of $0''.2$ - $0''.3$ from the nucleus. The fit could be improved by positing different turnover radii and/or acceleration/deceleration laws for each quadrant. Also, the high velocity data points not fit by the model appear to be clouds that do not encounter any dense medium and maintained their acceleration. Nevertheless, our goal of being able to explain all the basic trends in the data with a simple model was accomplished. We have ruled out gravitational and constant velocity models. We show that a model where the NLR emission is produced by expansion of radio jet plasma away from the radio axis does not fit the data well.

An important observational result is that the two distinct methods of obtaining radial velocities each gave similar results. This has been shown previously for NGC 4151 (Hutchings et al. 1998, Kaiser et al. 2000). The slitless spectral procedure of obtaining radial velocities has proven to be a useful and efficient tool for quickly examining and mapping nearby galaxies with clumpy NLRs and ENLRs. We will take advantage of this

technique in the future to map the kinematics of the NLR in nine other Seyfert galaxies.

This work was supported by NASA Guaranteed Time Observer funding to the STIS Science Team under NASA grant NAG 5-4103 and by *HST*. Additional support for this work was provided by NASA through grant number HST-GO-08340.01-A from the Space Telescope Science Institute, which is operated by AURA, Inc., under NASA contract NAS5-26555.

REFERENCES

- Axon, D.J., Marconi, A., Capetti, A., Macchetto, F.D., Schreier, E., & Robinson, A. 1998, *ApJ*, 496, L75
- Bicknell, G.V., Dopita, M.A., Tsvetanov, Z.I., Sutherland, R.S. 1998, *ApJ*, 495, 680
- Capetti, A., Macchetto, F., Axon, D.J., Sparks, W.B., & Boksenberg, A. 1995, *ApJ*, 448, 600
- Collins, N.R., et al., 2001, in preparation
- Crenshaw, D.M., Kraemer, S.B. 2000, *ApJ*, 532, L101
- Crenshaw, D.M., Kraemer, S.B., Hutchings, J.B., Bradley, L.D., II, Gull, T.R., Kaiser, M.E., Nelson, C.H., Ruiz, J.R., Weistrop, D. 2000, *AJ*, 120, 1731
- Georgantopoulos, I., Papadakis, I., Warwick, R.S., Smith, D.A., Stewart, G.C., & Griffiths, R.G. 1999, *MNRAS*, 307, 815
- Griffiths, R.G., Warwick, R.S., Georgantopoulos, I., Done, C., & Smith, D.A. 1998, *MNRAS*, 298, 1159
- Hutchings, J.B., Crenshaw, D.M., Kaiser, M.E., Kraemer, S.B., Weistrop, D., Baum, S., Bowers, C.W., Feinberg, L.D., Green, R.F., Gull, T.R., Hartig, G.F., Hill, G., and Lindler, D.J. 1998, *ApJ*, 492, L115
- Kaiser, M.E., Bradley, L.D. II, Hutchings, J.B., Crenshaw, D.M., Gull, T.R., Kraemer, S.B., Nelson, C.H., Ruiz, J., and Weistrop, D. 2000, *ApJ*, 528, 260
- Kukula, M.J., Ghosh, T., Pedlar, A., Schilizzi, R.T., Miley, G.K., de Bruyn, A.G., & Saikia, D.J. 1993, *MNRAS*, 264, 893
- Kukula, M.J., Ghosh, T., Pedlar, A., & Schilizzi, R.T. 1999, *ApJ*, 518, 117
- Lindler, D. 1999, CALSTIS Ref. Guide (version 6.4; Greenbelt: NASA/GSFC)

- Nelson, C.H., Weistrop, D., Hutchings, J.B., Crenshaw, D.M., Gull, T.R., Kaiser, M.E.,
Kraemer, S.B., and Lindler, D. 2000, *ApJ*, 531, 257
- Peterson, B.M., Wandel, A. 2000, *ApJ*, 540, L13
- Pogge, R.W., & De Robertis, M.M. 1993, *ApJ*, 404, 563
- Sako, M., Kahn, S.M., Paerels, F., Liedahl, D.A. 2000, *ApJ*, 543, L115
- Schmidt, G.D., & Miller, J.S. 1985, *ApJ*, 290, 517
- Schmitt, H.R., & Kinney, A.L. 1996, *ApJ*, 463, 498
- Tifft, W.G., & Cocke, W.J. 1988, *ApJS*, 67, 1
- Winge, C., Axon, D.J., Macchetto, F.D., & Capetti, A. 1997, *ApJ*, 487, L121
- Winge, C., Axon, D.J., Macchetto, F.D., Capetti, A., & Marconi, A. 1999, *ApJ*, 519, 134

Table 1. Observations

Date ^a	Instrument	Root Name	Filter/Grating	Exposure (s)	Slit
1991 July 18 (A)	PC	W0MW0601T	F502N	1800	
1992 Dec 11 (A)	FOC	X14W0301T	F501N	1197	
1997 Oct 20 (A)	WFPC2	U2E62A01T	F606W	500	
2000 Jan 16 (N)	STIS	O5F403010	clear	20	open
2000 Jan 16 (N)	STIS	O5F403020	G430M	2154	open
2000 Aug 22 (N)	STIS	O5KS01010	G430L	1080	52"x0".1

^aA-Archival, N-New

Table 2. Modeling Parameters

Parameter	Symbol or constant value
Min & Max distance of cones (pcs)	Min. = 0 , Max = D
Min & Max half-opening angle	$\theta_{min}, \theta_{max}$
Inclination angle	i
Deprojected Maximum velocity of NLR gas (km s^{-1})	V_{max}
Velocity Laws	<i>Constant velocity (CV)</i> <i>Radial Acceleration (RA)</i> <i>Radial Acceleration plus Constant Deceleration (RA+CD)</i> <i>Constant Tangential Flow (CT)</i> <i>Gravitational Infall (GI)</i>
Center of Slit	Centered on optical continuum peak
Position angle of the long slit	$\sim 71^\circ$
Slit Width (in pixels)	$0''.1$

Table 3. Parameters of each best fit model

Parameter	CV	RA	RA+CD	CT
D (pcs)	80	80	80	80
$\theta_{min}, \theta_{max}$	15, 25	15, 25	15, 25	15, 25
i	5°	5°	5°	5°
V_{max} (km s ⁻¹)	1400	3000	1750	550

Fig. 1.— FOC image of the bright NLR clouds of Mrk 3. The position of the long slit is seen to pass through the nucleus, and through the clouds in spots. The cross depicts the position of the nuclear continuum center. The backward ‘S’ shape of the main clouds is seen.

Fig. 2.— STIS slitless spectrum showing the region around [O III] λ 5007. The horizontal axis is along the dispersion, while the vertical scale is the spatial axis. Note the high dispersions of the NLR clouds. The clouds are also shifted slightly along the dispersion axis, the shift allowing the radial velocity to be calculated. The fainter ENLR clouds can also be seen $\sim 1''$ above and below the NLR. Their dispersion can also be seen.

Fig. 3.— Radial velocities averaged over bright clouds in the long slit are shown plotted against their corresponding values obtained with the slitless spectrum. The error bars represent the standard deviations from the averages.

Fig. 4.— Radial velocities (with respect to systemic) averaged over each individual cloud vs each cloud’s distance from the optical continuum center. Standard deviations in the position and velocity averages are shown as the error bars. The slitless clouds (marked with open circles) include all clouds, including those not lying in the slit, and those extending out into the ENLR (from $1''.5$ west of the nucleus outwards, and from $1''.0$ east of the nucleus outwards).

Fig. 5.— This figure shows the positions in the sky of the clouds, with their radial velocity magnitudes symbolised by the size of the figure used to identify them. The blueshifted clouds are symbolized by a “+”, while redshifted clouds are an “x”. The radial velocity measurements are binned over each cloud. The ENLR clouds can be seen to be mostly redshifted. The long slit clouds are differentiated by being in boldface.

Fig. 6.— Same as Figure 5, but zoomed in on the NLR clouds.

Fig. 7.— Unbinned radial velocity of each row perpendicular to the dispersion direction plotted against the distance from the center. The slitless spectral data points plotted here are only those observed to lie within the slit. Errors are roughly equal to the size of the symbols.

Fig. 8.— Same as Fig. 7, but overlaid with the best fit model of the radial acc + constant decel model. Parameters of the model are given in Table 3.

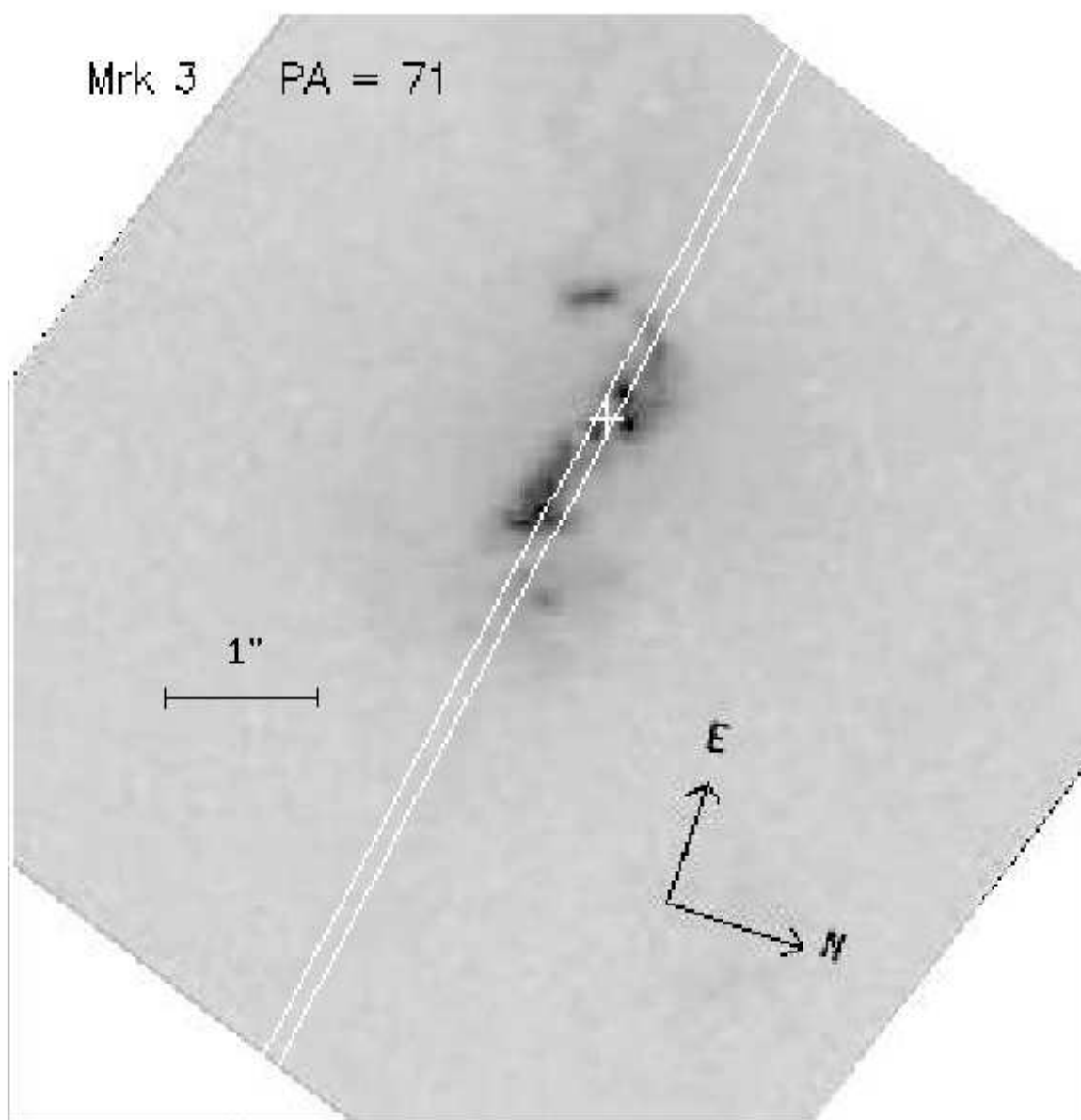


Fig. 1.

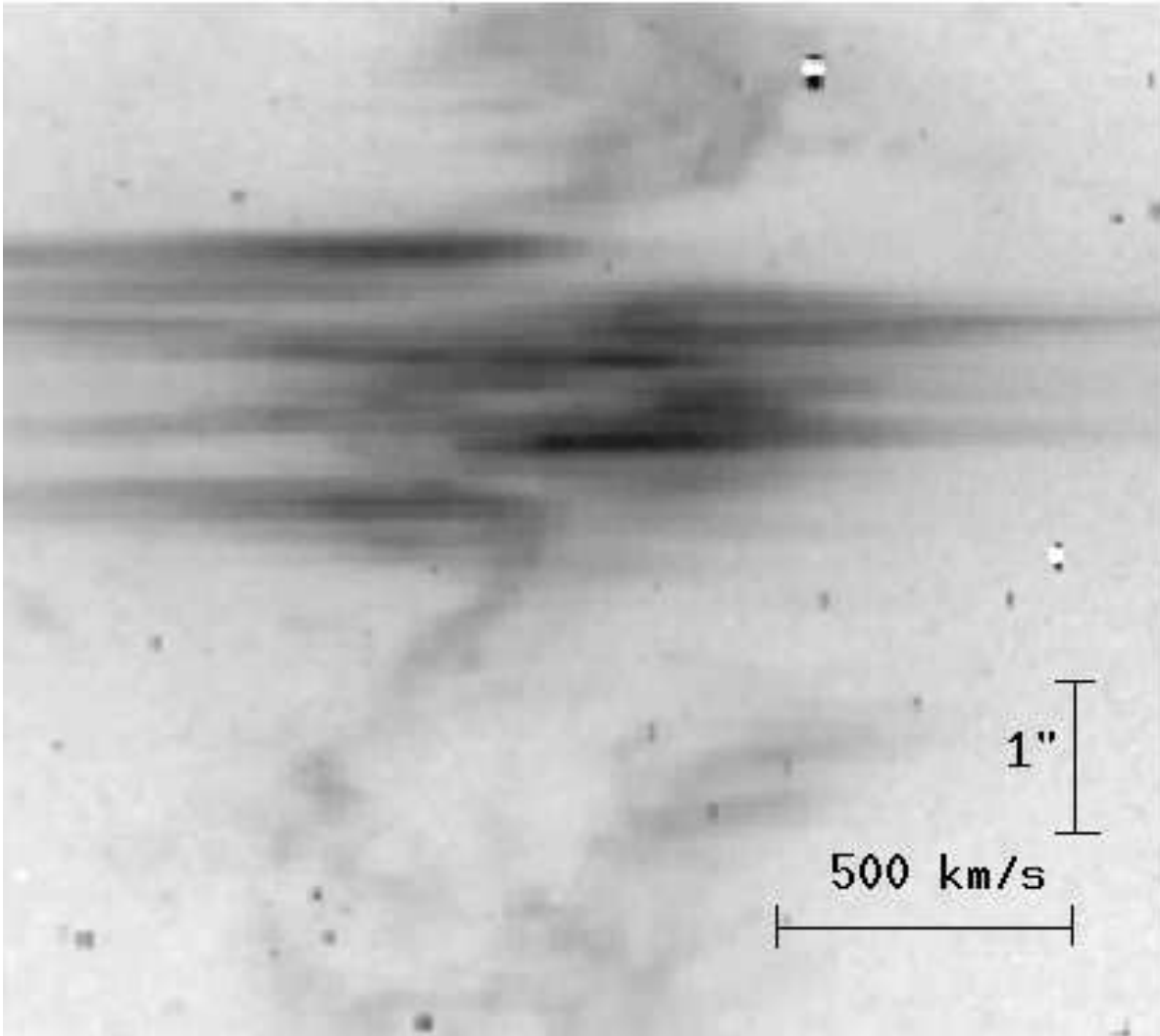


Fig. 2.

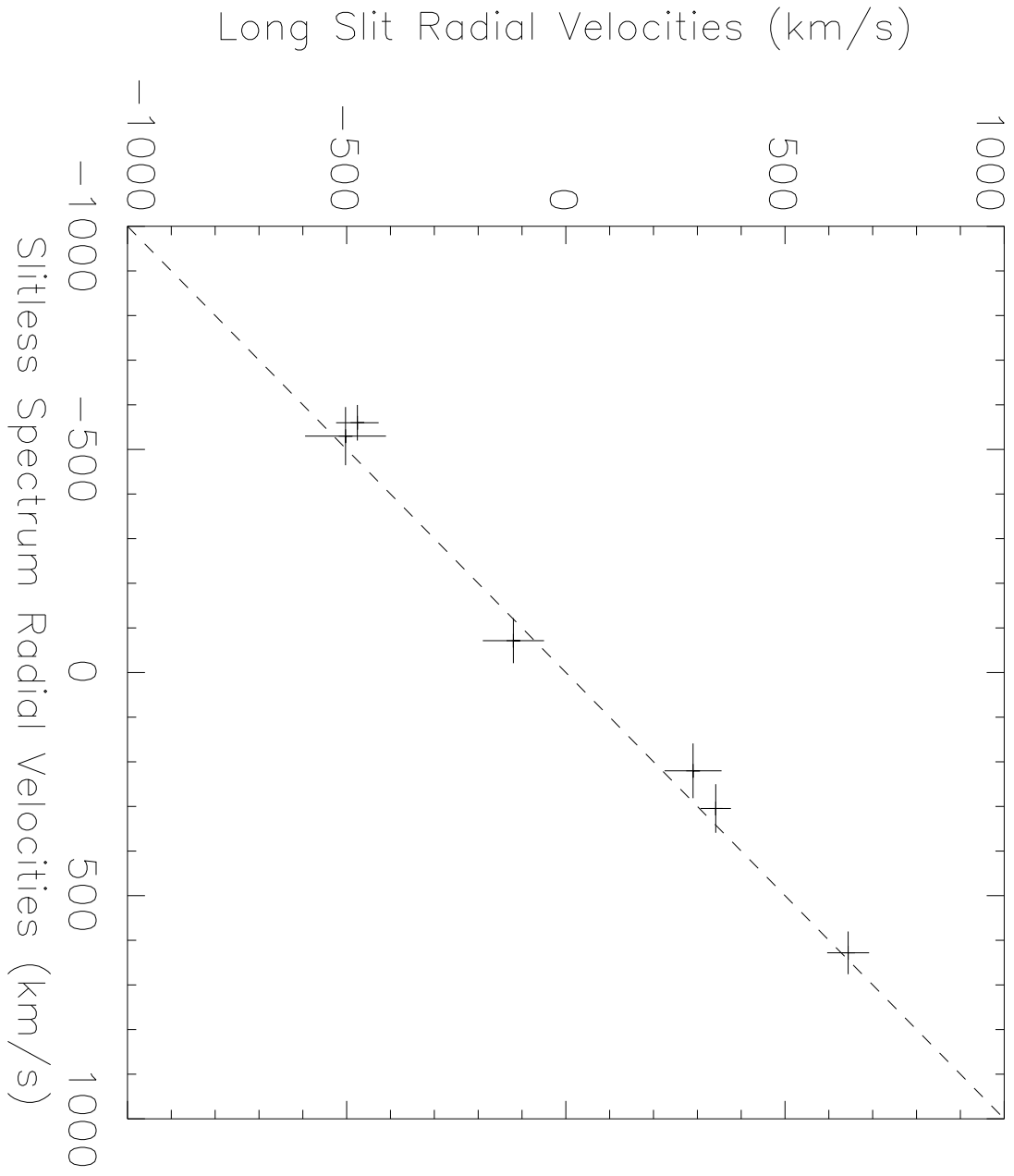


Fig. 3.

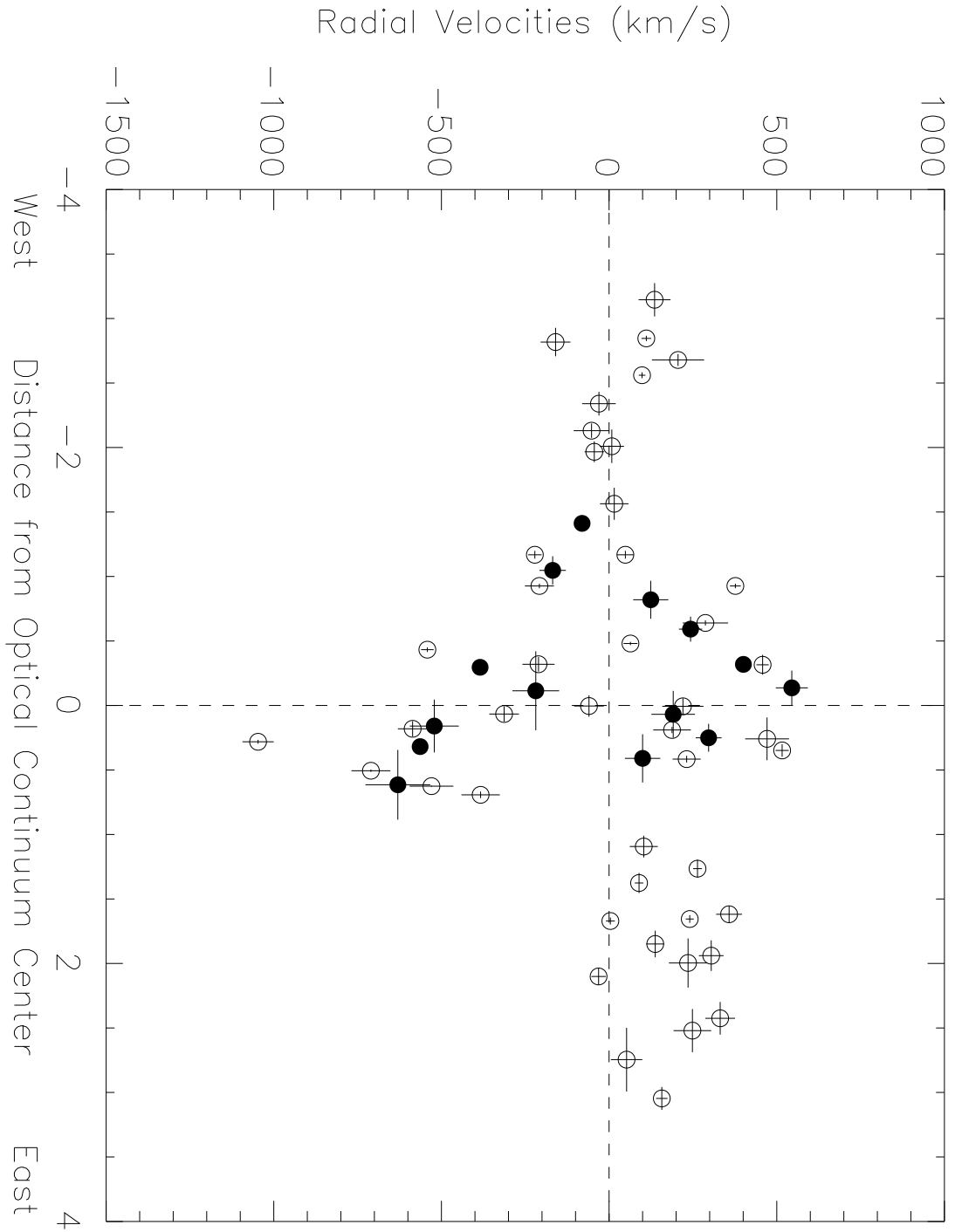


Fig. 4.

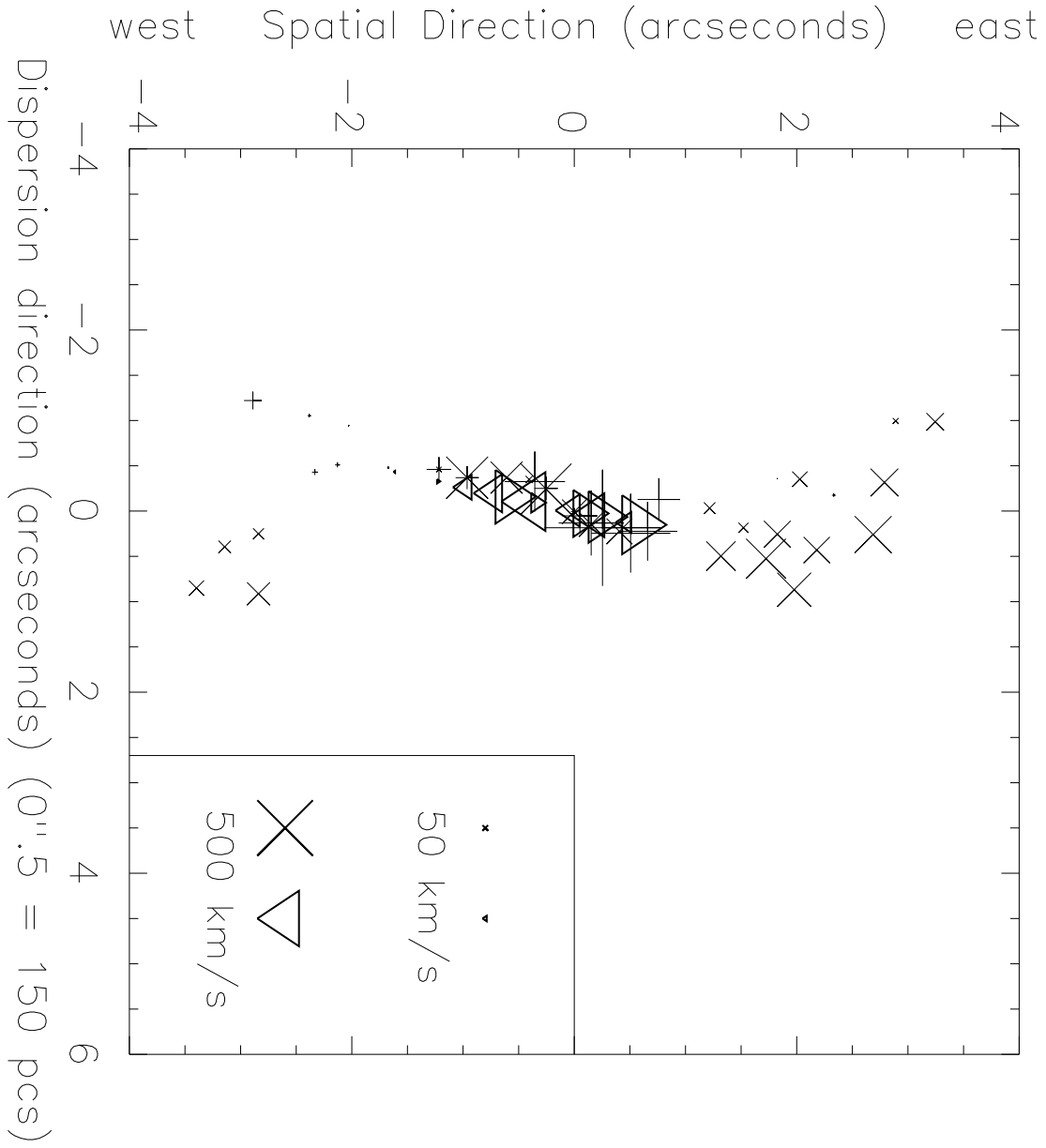
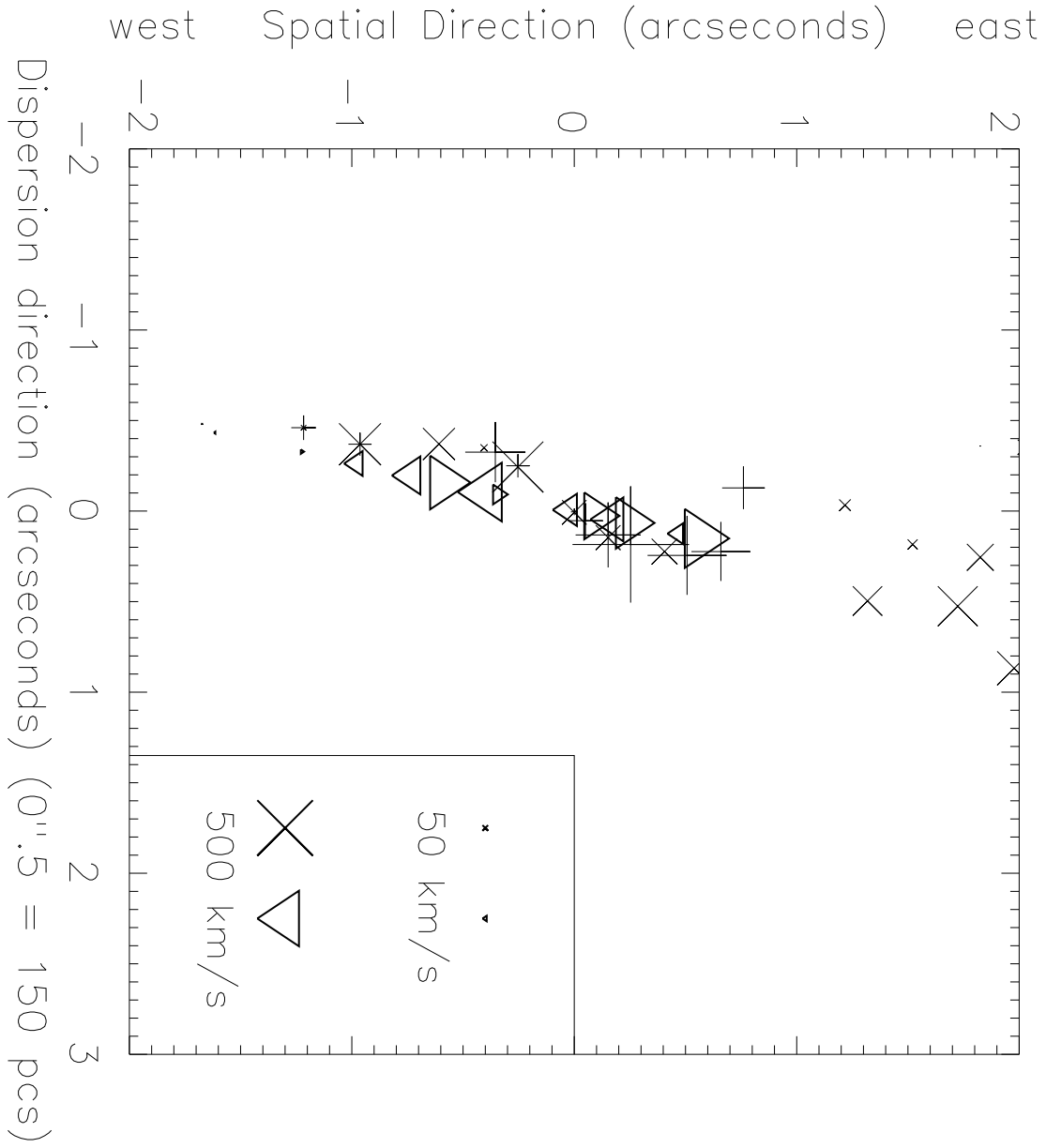


Fig. 5.



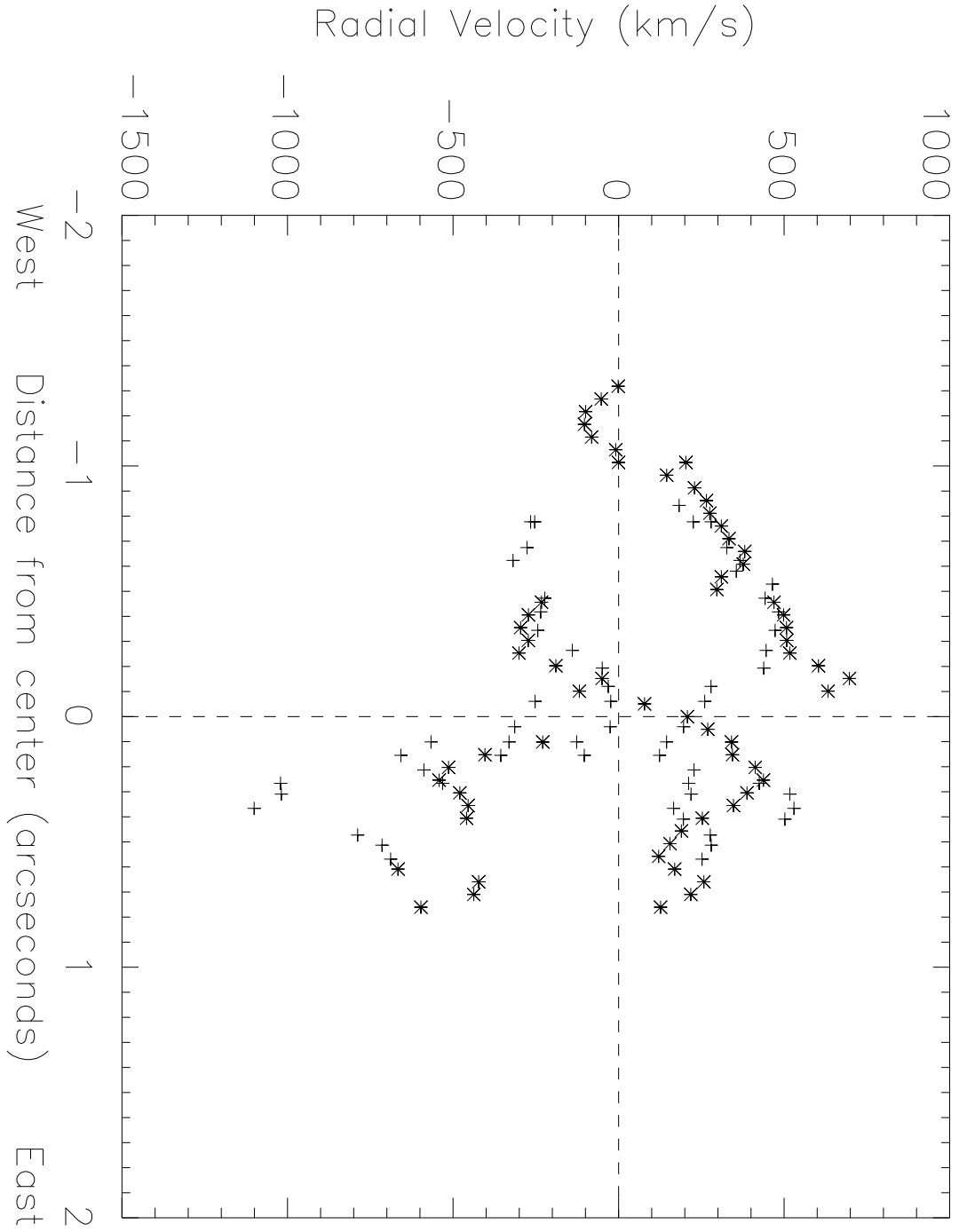


Fig. 7.

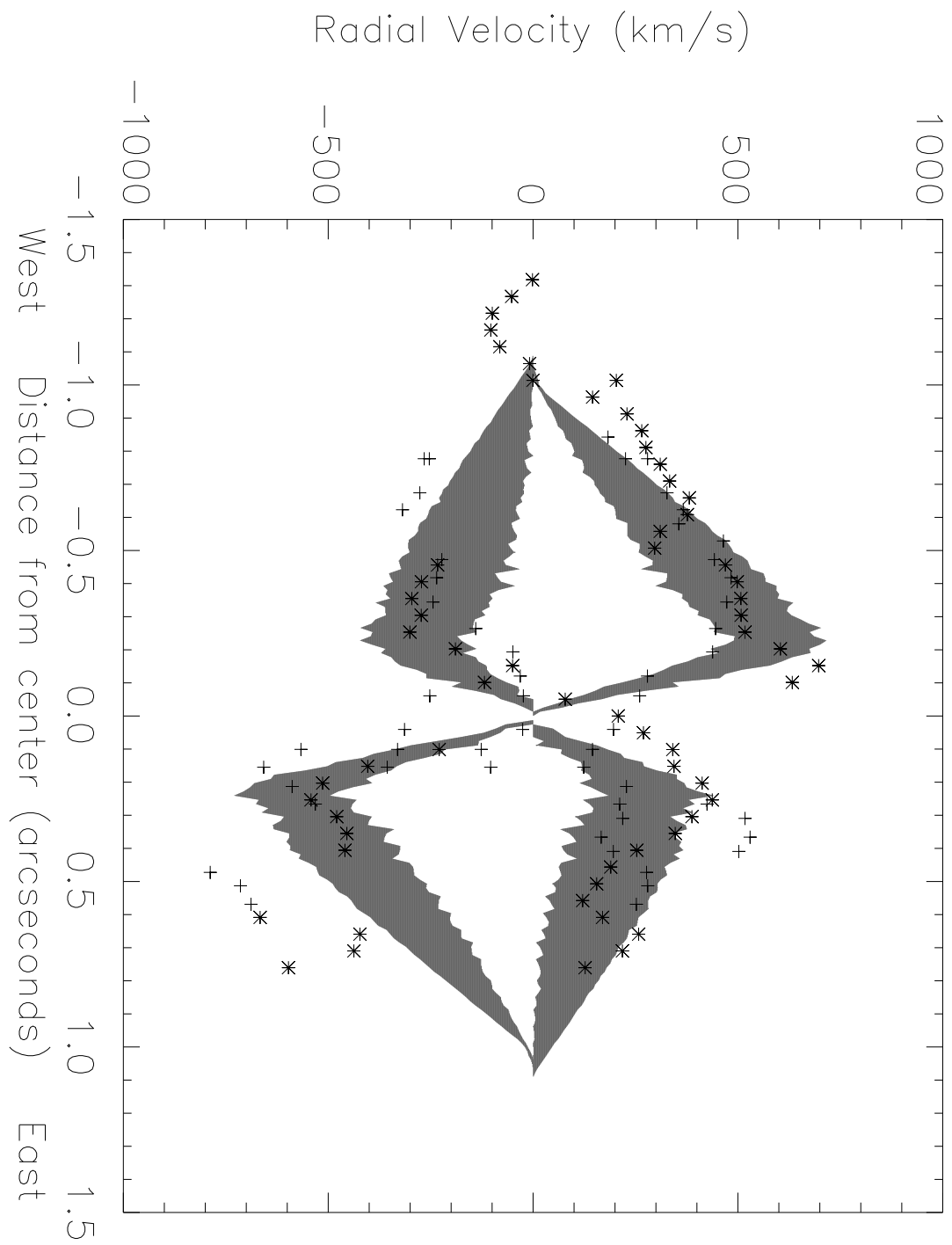


Fig. 8.